

Complex antiferromagnetic order in the metallic triangular lattice compound $\text{SmAuAl}_4\text{Ge}_2$


Keke Feng ^{1,2}, Caleb Bush,³ Olatunde Oladehin ^{1,2}, Minhyea Lee ⁴, and Ryan Baumbach ^{1,2}

¹Department of Physics, Florida State University, Tallahassee, Florida 32306, USA

²National High Magnetic Field Laboratory, Tallahassee, Florida 32310, USA

³Department of Physics, Rochester Institute of Technology, Rochester, New York 14623, USA

⁴Department of Physics, University of Colorado, Boulder, Colorado 80309, USA

 (Received 21 July 2023; revised 7 December 2023; accepted 5 January 2024; published 29 January 2024)

The compounds $Ln\text{AuAl}_4\text{Ge}_2$ ($Ln = \text{lanthanide}$) form in a structure that features two-dimensional triangular lattices of Ln ions that are stacked along the crystalline c axis. Together with crystal electric field effects, magnetic anisotropy, and electron-mediated spin exchange interactions, this sets the stage for the emergence of strongly correlated spin and electron phenomena. Here we investigate $\text{SmAuAl}_4\text{Ge}_2$, which exhibits weak paramagnetism that strongly deviates from conventional Curie-Weiss behavior. Complex antiferromagnetic ordering emerges at $T_{N1} = 13.2$ K and $T_{N2} = 7.4$ K, where heat capacity measurements show that these transitions are first and second order, respectively. These measurements also reveal that the Sommerfeld coefficient is not enhanced compared to the nonmagnetic analog $\text{YAuAl}_4\text{Ge}_2$, consistent with the charge carrier quasiparticles exhibiting typical Fermi liquid behavior. The temperature-dependent electrical resistivity follows standard metallic behavior, but linear magnetoresistance unexpectedly appears within the ordered state. We compare these results to other $Ln\text{AuAl}_4\text{Ge}_2$ materials, which have already been established as localized f -electron magnets that are hosts for interesting magnetic and electronic phases. From this, $\text{SmAuAl}_4\text{Ge}_2$ emerges as a complex quantum spin metal, inviting further investigations into its properties and the broader family of related materials.

DOI: [10.1103/PhysRevB.109.014436](https://doi.org/10.1103/PhysRevB.109.014436)

I. INTRODUCTION

Geometrically frustrated magnetic materials historically have attracted substantial interest as reservoirs for novel quantum phases [1–4]. A prototypical example is the insulating two-dimensional triangular antiferromagnetic spin lattice, where early theoretical efforts indicated that the ground state for spin $S = 1/2$ does not exhibit long-range order [5]. Later numerical studies modified this model by showing that 120° order can emerge when antiferromagnetic nearest-neighbor spin interactions are included [6–9]. Since then, substantial experimental studies have been carried out for insulators with triangular nets of transition metal elements, many of which exhibit complex magnetic phenomena [10–13]. Efforts have also been extended to lanthanide-containing systems, where the f -electron wave function is well localized by comparison to d -electron analogs. This results in weakened exchange couplings and large g factors, producing rich phase diagrams with easily tuned ground states, e.g., using magnetic fields [14,15]. More recently, related semimetal and metal systems have also been studied, where the presence of conduction electrons leads to long-range magnetic exchange interactions that are mediated by the Ruderman-Kittel-Kasuya-Yosida (RKKY) mechanism [16–18]. In addition to enhancing the degrees of freedom, this enables opportunities to explore the emergence of flat bands [19,20], exotic superconductivity [21,22], skyrmion phases [23], unconventional Hall effects [24,25], and potentially even metallic quantum spin liquids [26].

This motivated us to examine the compounds $LnT\text{Al}_4\text{Ge}_2$ ($Ln = \text{lanthanide}$ and $T = \text{transition metal}$), which feature triangular nets of Ln ions [27] (Fig. 1). Studies of the

$Ln = \text{Ce, Nd, Gd, and Tb}$ variants recently revealed complex ordering, indications of magnetic frustration, and complex temperature-magnetic field (T - H) phase diagrams. For example, $\text{CeAuAl}_4\text{Ge}_2$ hosts trivalent cerium moments with evidence for a ferromagnetic interaction within the triangular ab plane, which might relieve spin frustration [29]. In the case of $\text{NdAuAl}_4\text{Ge}_2$, the spins prefer to orient along the c axis, two magnetic phase transitions are observed ($T_{N1} = 1.75$ K and $T_{N2} = 0.49$ K), and several metamagnetic phase transitions are seen for magnetic fields applied along the c axis [30]. Even more complex behavior is seen for $\text{GdAuAl}_4\text{Ge}_2$ and $\text{TbAuAl}_4\text{Ge}_2$, which exhibit multiple transitions at substantially higher ordering temperatures, easy- ab -plane anisotropy, and multiple anisotropic metamagnetic phase transitions for magnetic fields applied in the triangular net plane [31,32]. Finally, it is noteworthy that $\text{CePtAl}_4\text{Ge}_2$ exhibits heavy-fermion antiferromagnetism, showing that Kondo lattice physics impacts behavior in some cases [33]. Thus, it is natural to anticipate that further variation of the Ln ion could produce other novel phenomena resulting from the combination of crystal electric field effects, complex RKKY interactions, geometric frustration, and strong electronic correlations.

Here we focus on $\text{SmAuAl}_4\text{Ge}_2$, where the f -electron state is likely to be distinct from that of its lanthanide neighbors. In particular, samarium f electrons (i) can adopt either a divalent ($4f^6$; $J = 0$) or trivalent ($4f^5$; $J = 5/2$) configuration, with crystal electric field splitting; (ii) can hybridize with conduction electron states; and (iii) can exhibit Van Vleck paramagnetism due to the ground state ($J = 5/2$) and first excited state ($J = 7/2$) being separated by a relatively small

energy [34,35]. This generates interesting behavior in other model systems, including (i) heavy-fermion ground states in $\text{SmOs}_4\text{Sb}_{12}$ [36,37], $\text{SmPt}_4\text{Ge}_{12}$ [38], and $\text{SmTi}_2\text{Al}_{20}$ [39]; (ii) topological Kondo insulating behavior in SmB_6 [40,41]; (iii) the coexistence of superconductivity and magnetism in SmRh_4B_4 [42]; and (iv) valence instabilities in samarium monochalcogenides [43].

From magnetization, heat capacity, and electrical transport measurements, we show that $\text{SmAuAl}_4\text{Ge}_2$ exhibits strong deviations from conventional Curie-Weiss paramagnetism at elevated temperatures due to crystal electric field splitting of the $J = 5/2$ multiplet and possibly other effects. Complex antiferromagnetic ordering appears at $T_{N1} = 13.2$ K and $T_{N2} = 7.4$ K, which are first- and second-order transitions, respectively. Metallic behavior without evidence for enhanced mass charge carrier quasiparticles is seen in the electronic coefficient of the heat capacity and electrical transport measurements, resembling what is seen for the nonmagnetic analog $\text{YAuAl}_4\text{Ge}_2$. Interestingly, although applied magnetic fields up to 9 T have little effect on the ordering temperatures, linear magnetoresistance resembling what is seen for $\text{GdAuAl}_4\text{Ge}_2$ and $\text{TbAuAl}_4\text{Ge}_2$ [31,32] is observed within the ordered state. Thus, $\text{SmAuAl}_4\text{Ge}_2$ emerges as an intriguing addition to the $\text{LnAuAl}_4\text{Ge}_2$ family, where complex magnetic ordering and unusual magnetotransport behavior are observed within an ensemble of f -electron spins whose high-temperature paramagnetism differs significantly from other Ln analogs.

II. EXPERIMENTAL METHODS

$\text{SmAuAl}_4\text{Ge}_2$ single crystals were grown using an aluminum molten metal flux following the procedure detailed in Refs. [27,29]. In order to allow comparison to a non- f -electron-containing analog, single-crystal specimens of $\text{YAuAl}_4\text{Ge}_2$ were produced using the same method. Crystals typically form as three-dimensional clusters, where individual crystals with dimensions on the order of 2 mm and hexagonal or triangular facets associated with the ab plane can be isolated (Fig. 1). Room temperature powder x-ray diffraction (XRD) measurements were performed using a Rigaku SmartLab SE x-ray diffractometer with a $\text{Cu } K\alpha$ source. The Rietveld refinement analysis was done using GSAS-II to assess the purity and determine the structure parameters. The principal c axis was identified by measuring the diffraction pattern on polished flat crystals using the same system and was also apparent in the crystal shape.

Temperature T dependent magnetization M measurements were carried out for $T = 1.8$ –300 K under magnetic fields of $\mu_0 H = 0.5$ T applied parallel (\parallel) and perpendicular (\perp) to the crystallographic c axis using a Quantum Design vibrating-sample magnetometer magnetic property measurement system. Data were collected (i) under zero-field-cooled (ZFC) conditions, where the sample was cooled to $T = 1.8$ K, the magnetic field was applied, and M was measured as T increased to 300 K, and (ii) field-cooled (FC) conditions, where the magnetic field was applied at 300 K and M was measured as T decreased to 1.8 K. Isothermal magnetization measurements were also performed for $\mu_0 H \leq 7$ T, where the sample was zero field cooled prior to the measurement at each

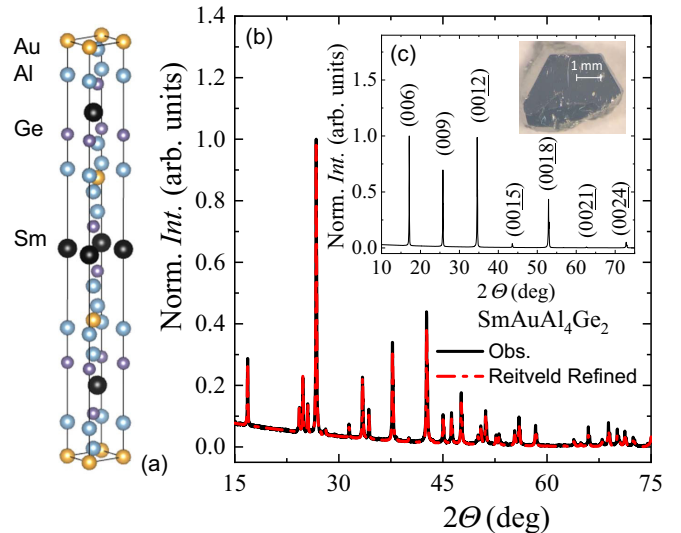


FIG. 1. (a) Crystal structure of $\text{SmAuAl}_4\text{Ge}_2$ [28]. (b) Rietveld refinement of the powder x-ray diffraction pattern for $\text{SmAuAl}_4\text{Ge}_2$. The black line is the observed experimental pattern, and the red dashed line is the calculated pattern. Inset: A single-crystal specimen obtained from the aluminum flux growth method described in the text. (c) XRD patterns of a c -axis-aligned $\text{SmAuAl}_4\text{Ge}_2$ single crystal similar to that shown in the inset.

temperature. Heat capacity C measurements were performed for $T = 1.8$ –40 K in a Quantum Design physical properties measurement system using a conventional thermal relaxation technique. Electrical resistivity ρ measurements for $T = 1.8$ –300 K and magnetic fields $\mu_0 H \leq 9$ T were performed in a four-wire configuration for polished single crystal using the same system. For $\rho(T)$, both ZFC and FC measurements were performed. For $\rho(H)$, samples were zero field cooled prior to measurements.

III. RESULTS

The trigonal $\text{SmAuAl}_4\text{Ge}_2$ unit cell is shown in Fig. 1(a). The powder x-ray diffraction pattern for $\text{SmAuAl}_4\text{Ge}_2$ is shown in Fig. 1(b), where the data are described by the trigonal $\text{LnAuAl}_4\text{Ge}_2$ structure (space group $R\bar{3}m$, No. 166 [27]). Rietveld refinement yields lattice parameters and unit cell volume $a = 4.21711(10)$ and $31.1452(6)$ Å and $V = 479.680(13)$, consistent with expectations for the trivalent lanthanide contraction for $\text{LnAuAl}_4\text{Ge}_2$ discussed in Ref. [31]. Other fit parameters are summarized in Table I. Figure 1(c) shows the XRD pattern for a c -axis-aligned crystal of $\text{SmAuAl}_4\text{Ge}_2$, exhibiting only the $(00l)$ diffraction peaks. This reveals that the naturally occurring hexagonal facets are aligned in the ab plane.

The temperature-dependent magnetic susceptibilities for magnetic fields $\mu_0 H$ applied parallel [$\chi_{\parallel}(T)$] and perpendicular [$\chi_{\perp}(T)$] to the crystallographic c axis for $\text{SmAuAl}_4\text{Ge}_2$ are shown in Fig. 2. Weak easy ab -plane anisotropy is observed in the paramagnetic state, where (i) $\chi_{\parallel}(T)$ initially decreases with decreasing T , evolves through a broad minimum centered near 175 K, and exhibits a gradual increase down to 20 K and (ii) $\chi_{\perp}(T)$ weakly decreases below 300 K, goes through

TABLE I. Summary of crystallographic parameters resulting from Rietveld refinement of the data using GSAS-II. Fits yielded the lattice constants $a = 4.21711(10)$ and $31.1452(6)$ Å and $V = 479.680(13)$. The quality of the fit is characterized by $R_w = 7.76$.

| Site label | x, y, z | Occupancy | U_{iso} |
|------------|---------------|-----------|-----------|
| Al2 | 0, 0, 0.08089 | 1 | 0.0199 |
| Ge | 0, 0, 0.22380 | 1 | 0.0136 |
| Al1 | 0, 0, 0.31009 | 1 | 0.0538 |
| Sm | 0, 0, 0.50000 | 1 | 0.0027 |
| Au | 0, 0, 0 | 1 | 0.0018 |

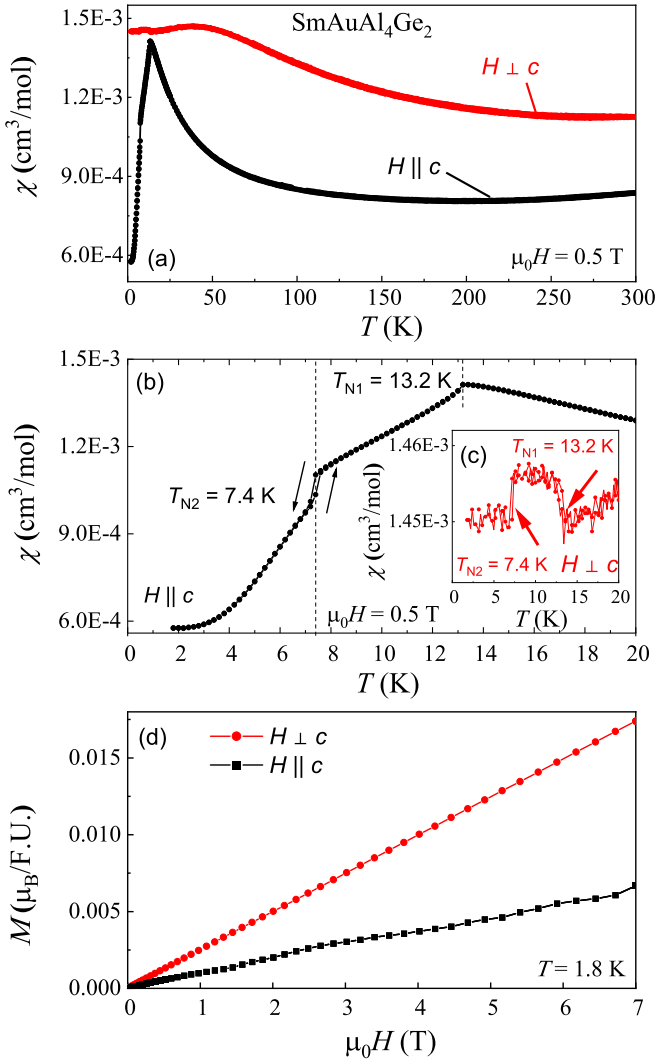


FIG. 2. (a) Temperature-dependent magnetic susceptibility $\chi(T)$ for SmAuAl₄Ge₂ for magnetic fields $\mu_0 H = 0.5$ T applied parallel (\parallel) and perpendicular (\perp) to the c axis. Data were collected both for zero field cooling and field cooling, as described in Sec. II. Zoom of $\chi(T)$ at low temperatures for magnetic fields $\mu_0 H = 0.5$ T applied (b) parallel and (c) perpendicular to the c axis, emphasizing the magnetic phase transitions. The dotted vertical lines in (b) represent the locations of the ordering temperatures T_{N1} and T_{N2} . (d) Isothermal magnetization $M(H)$ for both field directions at $T = 1.8$ K.

a broad minimum near 250 K, and exhibits a broad maximum centered around 50 K. This behavior is distinct from what is seen for other lanthanides with localized f states but resembles results for some samarium-containing intermetallics and points towards the samarium ions having a trivalent f -electron configuration where the $J = 5/2$ multiplet is strongly impacted by crystal electric field splitting below 300 K.

Antiferromagnetic phase transitions emerge near $T_{N1} = 13.2$ K and $T_{N2} = 7.4$ K. The details of this behavior are shown in Figs. 2(b) and 2(c), where $\chi_{\parallel}(T)$ is strongly reduced following each transition and weak hysteresis is observed around T_{N2} . The origin of the hysteresis is not obvious, but we speculate that it indicates the formation of history-dependent magnetic domains within the ordered state. In contrast, $\chi_{\perp}(T)$ weakly increases and then decreases at T_{N1} and T_{N2} , respectively. These trends reveal that the magnetic ordering is characterized by progressively strengthening antialignment of the spins along the c axis, with a weak coalignment of spins at T_{N1} and a weak antialignment at T_{N2} for the in-plane configuration. The occurrence of multiple phase transitions resembles what is seen for $LnAuAl_4Ge_2$ analogs that exhibit conventional Curie-Weiss magnetism [31,32], indicates the presence of competing magnetic exchange interactions, and further clarifies how the magnetic anisotropy varies with Ln . To further investigate the ordered state, isothermal magnetization measurements were performed at $T = 1.8$ K. As seen in Fig. 2(c), $M(H)$ increases linearly with $\mu_0 H \leq 7$ T, with no evidence for metamagnetic phase transitions for both field directions. This contrasts with what is seen for the $Ln = Nd, Gd,$ and Tb analogs, which all show a rich variety of anisotropic metamagnetic phase transitions. Evidence for quantum oscillations is also seen for $H \parallel c$, indicating the high quality of these crystals.

The heat capacity divided by temperature C/T data for SmAuAl₄Ge₂ are compared to those of the $J = 0$ nonmagnetic analog YAuAl₄Ge₂ in Fig. 3. As expected, there are qualitative similarities between these curves at elevated temperatures where phonons dominate C/T , although the Sm curve lags behind the Y curve with decreasing temperature. Similar behavior is observed in other lanthanide series when the mass of the non- $4f$ ion differs from that of the $4f$ ion [44]. To account for this difference, fits to the data (dashed lines) were done using the expression

$$C(T) = \gamma T + C_{\text{Debye}}, \quad (1)$$

where γ is the electronic coefficient of the heat capacity and C_{Debye} is the Debye integral function. These fits yield $\gamma \approx 5$ mJ mol⁻¹ K⁻² for both compounds and Debye temperatures $\theta_D = 242$ and 220 K for YAuAl₄Ge₂ and SmAuAl₄Ge₂, respectively. These γ values resemble what was seen for the Gd and Tb analogs [31,32], indicating that the electronic band states are similar, and the primary factors that lead to differences in the heat capacities are the distinct f -electron states that are seen for different lanthanides.

There are two pronounced peaks in $C(T)$ at T_{N1} and T_{N2} . The feature at T_{N1} is sharp and abrupt, and an examination of the heat pulse relaxation curve $T(t)$ reveals evidence of latent heat, as expected for a first-order phase transition [Fig. 3(c)]. To account for this, in the vicinity of T_{N1} , the data were

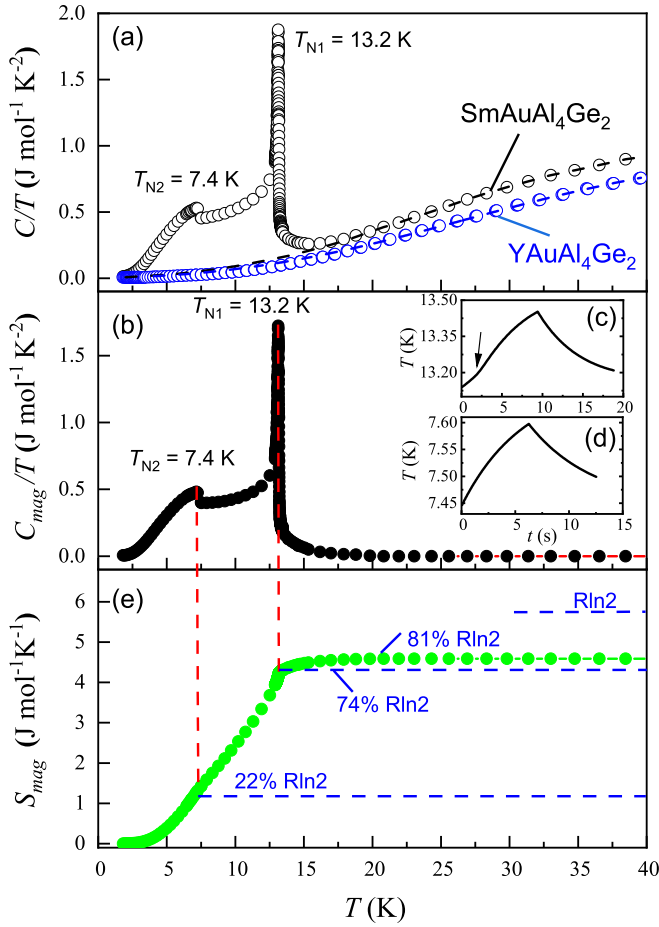


FIG. 3. (a) The heat capacity divided by temperature C/T vs T for single-crystal $\text{SmAuAl}_4\text{Ge}_2$ and $\text{YAuAl}_4\text{Ge}_2$ at $T = 1.8\text{--}40$ K. The dotted lines represent the fits that are described in the text. (b) The magnetic heat capacity divided by temperature C_{mag}/T vs T plotted for $\text{SmAuAl}_4\text{Ge}_2$. The relaxation curves around (c) T_{N1} and (d) T_{N2} . In (c), the arrow indicates the kink in the heating curve due to the latent heat of the first-order phase transition. A similar feature is not detected around T_{N2} . (e) Magnetic entropy S_{mag} vs T , which is obtained from the heat capacity data as described in the text.

analyzed using a single slope expression [45], resulting in the curve shown in Fig. 3. For the peak near T_{N2} , the relaxation curves indicate that it is second order [Fig. 3(d)]. To determine the magnetic contribution to the entropy $S_{\text{mag}}(T)$ [Fig. 3(e)], we isolate the magnetic contribution to the heat capacity [$C_{\text{mag}}/T = C_{\text{Sm}}/T - (\gamma T + C_{\text{D}}/T)$] and then integrate it [$S_{\text{mag}}(T) = \int_0^T C_{\text{mag}}/T dT$]. $S_{\text{mag}}(T)$ reaches $4.28 \text{ J mol}^{-1} \text{ K}^{-1}$ at T_{N1} , which is 74% of the value expected for a doublet ground state ($R \ln 2$) and is strongly reduced from the full $J = 5/2$ value ($R \ln 6$). This is consistent with the perspective from $\chi(T)$ measurements that crystal electric field splitting impacts the low-temperature f -state behavior. However, we also note that despite the good agreement between C/T and the Debye fit, the finding that $S_{\text{mag}} < R \ln 2$ may imply that phonon background subtraction is an overestimate. As described below, crystal electric field splitting plays an important role in this temperature range, which is not considered in this analysis of the data.

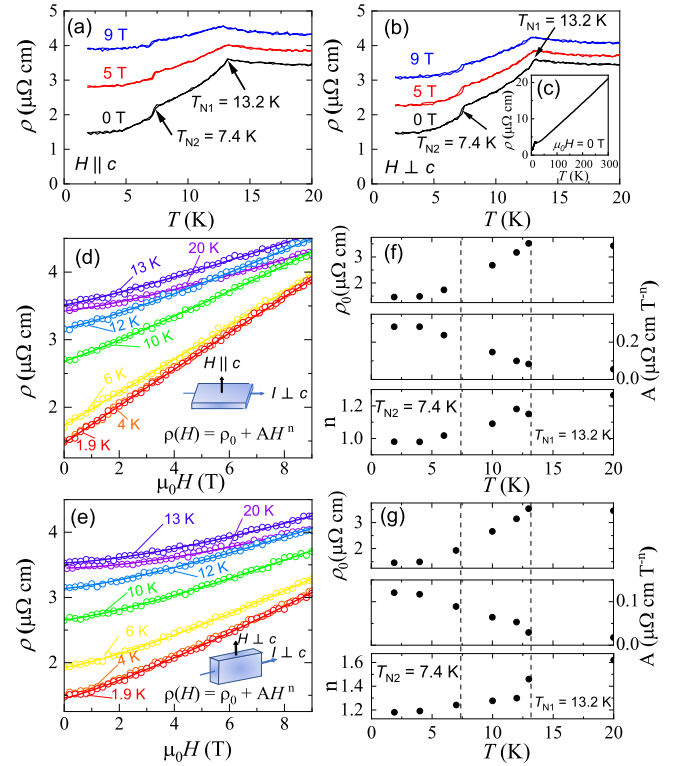


FIG. 4. Electrical resistivity $\rho(T)$ of $\text{SmAuAl}_4\text{Ge}_2$ near T_{N1} and T_{N2} shown at different applied fields (a) along the c axis and (b) perpendicular to the c axis. Data were collected both for zero field cooling and field cooling. (c) $\rho(T)$ for $1.8 < T < 300$ K. Isothermal magnetoresistance $\rho(H)$ at different temperatures for magnetic field applied (d) along the c axis ($H \parallel c$) and (e) perpendicular to the c axis ($H \perp c$). The electrical current remains in the ab plane for both cases. The insets show the schematics of the measurement configurations. The data points are represented by open circles, and the fits are shown as solid lines. (f) and (g) The temperature dependence of parameters ρ_0 , A , and n resulting from fits to the data in (d) and (e), respectively. The dotted vertical lines represent the locations of the ordering temperatures T_{N1} and T_{N2} .

Figures 4(a)–4(c) show the temperature-dependent electrical resistivity $\rho(T)$ with the electrical current I applied in the ab plane and magnetic fields applied either in the ab plane or along the c axis. Consistent with the metallic behavior that is observed for other lanthanide variants [31,32], the room temperature resistivity is near $20 \mu\Omega \text{ cm}$ and decreases with decreasing T . At low temperatures, the magnetic ordering is preceded by a weak minimum that is centered near 20 K. Similar behavior was seen for $\text{GdAuAl}_4\text{Ge}_2$ [31], where it is associated with spin fluctuation scattering. Following this, the transitions at T_{N1} and T_{N2} both reduce $\rho(T)$ due to the removal of spin disorder scattering. $\rho(T)$ finally saturates towards a value near $1.5 \mu\Omega \text{ cm}$ at low temperatures, showing that there is little disorder due to crystalline defects. The influence of a magnetic field applied for $H \parallel$ and $\perp c$ is shown in Figs. 4(a) and 4(b). Although the overall value of $\rho(T)$ is enhanced with increasing field, the ordering temperatures remain nearly constant.

Figures 4(d) and 4(e) show the magnetoresistance $\rho(H)$ for electrical current I applied in the ab plane with $H \parallel$ and

TABLE II. Summary of values obtained from fits to the magnetic susceptibility $\chi(T)$ data using Eq. (2).

| | χ_0 ($\text{cm}^3 \text{mol}^{-1}$) | θ (K) | μ_{eff}/μ_B | C_0 (emu K mol^{-1}) | ν |
|--------------------|--|--------------|--------------------------|-----------------------------------|-------|
| χ_{\perp} | 9.50×10^{-4} | -16.3 | 0.62 | 3.06×10^{-2} | 0.73 |
| χ_{\parallel} | 7.05×10^{-4} | -13.8 | 0.35 | 3.06×10^{-2} | 0.41 |

\perp to the c axis. At the lowest temperatures, $\rho(H)$ is roughly linear over a wide range of fields for $H \parallel c$, with no evidence for metamagnetic phase transitions. $\rho(H)$ subsequently develops weak positive curvature as the temperature is raised through T_{N1} and T_{N2} . As noted previously for $\text{GdAuAl}_4\text{Ge}_2$ and $\text{TbAuAl}_4\text{Ge}_2$ ($I \parallel ab$, $H \parallel c$), this differs from the conventional quadratic magnetoresistance associated with orbital charge carriers' motion and suggests the presence of an unconventional scattering process [32]. In contrast, $\rho(H)$ for $H \perp c$ exhibits positive curvature even at low temperatures, again without evidence of any metamagnetic phase transition. To quantify these behaviors, we carried out fits to the data using the power law expression $\rho(H) = \rho_0 + AH^n$, which accounts for the residual resistivity ρ_0 and the field dependence that arises from the combined electronic and magnetic scattering behaviors. For $H \parallel c$, as shown in Fig. 4 (f), n gradually increases from 1 to 1.3, indicating the persistence of a single dominant scattering mechanism. For $H \perp c$, as shown in Fig. 4(g), n initially gradually rises from a value near 1.2 until it abruptly increases near T_{N1} , presumably as a result of a change in the magnetic scattering.

IV. DISCUSSION

These data reveal that $\text{SmAuAl}_4\text{Ge}_2$ exhibits complex magnetic ordering that emerges from a non-Curie-Weiss paramagnetic state. In order to understand this, we first consider a minimal model for the paramagnetism which assumes both that the trivalent f -electron state ($4f^5$) dominates the magnetic phenomena and that the crystal electric field (CEF) splitting is sized such that it impacts $\chi(T)$ at and below room temperature. As discussed in Ref. [15], the standard Curie-Weiss-like temperature dependence $\chi(T) = C/(T - \theta)$ is valid only (i) if all of the crystal field split orbitals are homogeneously occupied or (ii) if $T \ll \Delta_0/k_B$ and the quadratic H dependence in the Zeeman splitting is negligible [15]. Condition (ii) is unique to $4f$ -electron systems, where the scale of Δ_0 (the lowest crystal electric field splitting energy) is significantly lower than that of $3d$ counterparts. In this situation, the magnetic susceptibility is given by the expression

$$\chi(T) = \chi_0 + \frac{\nu C_0}{T - \nu\theta}, \quad (2)$$

where C_0 is the Curie constant ($C_0 = \frac{N_A \mu_0 \mu_B^2 g_J^2}{k_B}$), θ is the Curie-Weiss temperature, and $\nu = g/g_J$ is a scaled Landé g factor ($g_J = \frac{2}{7}$). Fits to $\chi(T)$ using Eq. (2) are shown in Fig. 5, and the resulting parameters are summarized in Table II. Importantly, the fits are expected to work only before the first excited state begins to get populated, which is evidenced in the data by the broad maximum that appears in $(\chi_{\parallel} - \chi_0)^{-1}$ near 200 K. Based on this, the lower bound of Δ_0 can be

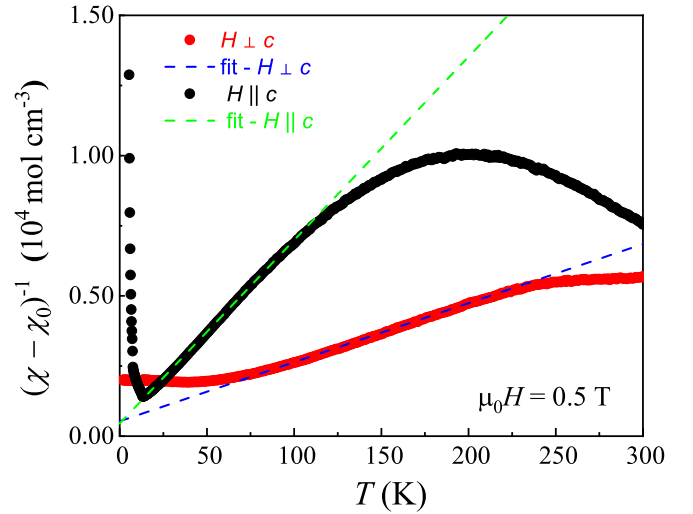


FIG. 5. Inverse magnetic susceptibilities $(\chi - \chi_0)^{-1}$ for $\text{SmAuAl}_4\text{Ge}_2$ and the fitting results of Eq. (2) (dashed line) are shown for both the $H \perp c$ and $H \parallel c$ configurations.

estimated to be on the order of a few tens of meV (a few hundred kelvin) [15]. Using the g factor found from the fit, the effective moment $\mu_{\text{eff}} = g\mu_B\sqrt{J(J+1)}$ (where total angular momentum $J = 5/2$ was used for Sm^{3+}) is found to be $0.62\mu_B$ and $0.35\mu_B$ for $H \parallel$ and \perp to c , respectively. These values are slightly reduced from the full Sm^{3+} value of $0.85\mu_B$ [46], and the differing values of μ_{eff} are associated with the anisotropy of the ν values. Finally, the negative Curie-Weiss temperatures indicate the presence of antiferromagnetic spin exchange interactions.

While this picture qualitatively describes the data, several features also deviate from it. First, we note that $1/\chi_{\perp}(T)$ is strongly suppressed from the fit values below 70 K. The reason for this is not clear, but we speculate that it might be attributed to anisotropic spin fluctuations in the vicinity of ordering temperature, e.g., related to spin frustration in the ab plane. It is also important to note that different minima in $\chi(T)$ are observed for the two field directions. This is unexpected since CEF splitting in zero field is isotropic and thus should impact both curves in similar ways. This implies that additional effects (e.g., Van Vleck splitting between the $J = 5/2$ and $7/2$ states) may need to be considered to fully understand this unusual paramagnetic state. A spectroscopy study such as inelastic neutron scattering would be useful to render an accurate CEF characterization.

This behavior contrasts with what is seen for other $\text{LnAuAl}_4\text{Ge}_2$ analogs with conventional Curie-Weiss paramagnetism (Table III) and might lead to the expectation that the ground state will show distinct behavior. Despite this, there are noteworthy similarities in the ordered states between $\text{SmAuAl}_4\text{Ge}_2$ and its analogs. This is highlighted in Fig. 6, where we plot the ordering temperatures for several examples ($\text{Ln} = \text{Ce}, \text{Nd}, \text{Sm}, \text{Gd}, \text{Tb}, \text{and Dy}$) and the de Gennes scaling factor [$G = (g_J - 1)^2 J(J + 1)$] vs lanthanide [48,49]. From this, it is clear that there is close agreement between G and the trends seen in the ordering temperatures, indicating that these compounds have a shared spin exchange mechanism. An explanation for this could be that while each

TABLE III. Summary of magnetic properties for $LnAuAl_4Ge_2$ (Ln = lanthanide) obtained from the magnetic susceptibility $\chi(T)$, magnetization $M(H)$, and heat capacity $C(T)$, where $\chi(T)$ was collected at $\mu_0H = 0.5$ T and M values here are reported at 7 T and 1.8 K. Magnetic entropy $S_{\text{mag}}(T)$ is calculated from $C_{\text{mag}}(T)$ (see text). T_{N1} , T_{N2} , and T_{N3} refer to the zero-field ordering temperatures identified from $\chi(T)$. \perp (\parallel) refers to $H \perp c$ ($H \parallel c$). R refers to the gas constant, and J is the total angular momentum for each Ln^{3+} ion. Data for $Ln = Ce$, Nd, Gd, and Tb are from Refs. [29–32].

| | Ce [29] | Nd [30] | Sm | Gd [31] | Tb [31] |
|--|---------|--------------------------|-----------------------|---------------------|---------------------|
| T_{N1} (K), ZFC | 1.40 | 1.75 | 13.2 | 17.8 | 13.9 |
| T_{N2} (K), ZFC | | 0.49 | 7.4 | 15.6 | 9.8 |
| T_{N3} (K), ZFC | | | | 13.8 | |
| Anisotropy | 0.3 | 1.62 | 2.53 | 1.56 | 5.9 |
| $\chi_{\parallel}/\chi_{\perp}$ at 1.8 K | | | | | |
| H_{C1} (T) | | 0.04 ($H \parallel c$) | | 1.9 ($H \perp c$) | 1.3 ($H \perp c$) |
| H_{C2} (T) | | 0.75 ($H \parallel c$) | | | 1.9 ($H \perp c$) |
| H_{C3} (T) | | 1.6 ($H \parallel c$) | | | 2.7 ($H \perp c$) |
| M_{\perp} (in units of μ_B) | 1.3 | 1.23 | 1.74×10^{-2} | 4.9 | 8.31 |
| M_{\parallel} (in units of μ_B) | 0.4 | 1.41 | 6.7×10^{-3} | 3.65 | 1.33 |
| $S_{\text{mag}}(T = T_{N1})$ (J mol $^{-1}$ K $^{-1}$) | 3.00 | 3.46 | 4.28 | 12.8 | 13.9 |
| $S_{\text{mag}}(T = 70$ K) (J mol $^{-1}$ K $^{-1}$) | | 14 | 0.56 | 16.4 | 20.7 |
| $R\ln(2J + 1)$ (J mol $^{-1}$ K $^{-1}$) | 14.9 | 19.1 | 14.9 | 17.3 | 21.3 |

of these compounds has a different CEF splitting for the f -electron state, which impacts the effective magnetic moment, they all share similar Fermi surface topographies. This would result in them having similar conduction electron-mediated RKKY spin interactions that are robust against variations of the lanthanide ion. Indeed, this is expected in the absence of hybridization between the f and conduction electrons.

Another important distinction between $SmAuAl_4Ge_2$ and its relatives is the lack of metamagnetic phase transitions. This is puzzling, but given that the $M(H)$ curves for $SmAuAl_4Ge_2$ are nonsaturating at 7 T, one possibility is that they will appear at fields larger than those accessed in this study. The

reason for this might be that the relatively small Sm magnetic moment modifies the internal field in a way that enhances the field-driven transition energy scale. Alternatively, it is possible that both measured directions represent hard magnetic axes. More detailed measurements (e.g., exploring the in-plane magnetic anisotropy) would be useful for addressing this question.

It is also appealing to consider that the RKKY interaction alone may not fully account for the complex magnetic order. All of these compounds, with the exception of $CeAuAl_4Ge_2$, exhibit multiple temperature- and field-dependent transitions, indicating the presence of magnetic frustration. This motivates the need for further work to understand effects arising from (i) competing RKKY interactions, e.g., as seen for the anisotropic next-nearest-neighbor Ising model [50], and (ii) geometric frustration. In any case, these behaviors open an intriguing path for stabilizing and tuning nontrivial spin states similar to what is seen for the structurally similar Gd_2PdSi_3 [23], where a unique combination of spin anisotropy with a centrosymmetric triangular Gd lattice produces an unusual skyrmion state. For the $LnAuAl_4Ge_2$ compounds, if skyrmions or other nontrivial magnetic textures do not appear in the T - H phase diagram of one of the parent compounds, it may be possible to access them by chemically mixing the f -element site. This would preserve the structural constraints but vary the magnetic anisotropy, magnetic moment, and the resulting T - H phase diagrams.

Finally, it is intriguing that linear magnetoresistance is seen for fields applied along the c axis. This is similar to what is seen for the Gd and Tb analogs [32], and based on this commonality, we infer that the underlying origin of this behavior is independent of the details of the f -electron state. This naturally leads us to consider that it is connected to electronic degrees of freedom that are shared among all of the chemical analogs. As we noted previously, a possible scenario is that the formation of charge or spin density waves

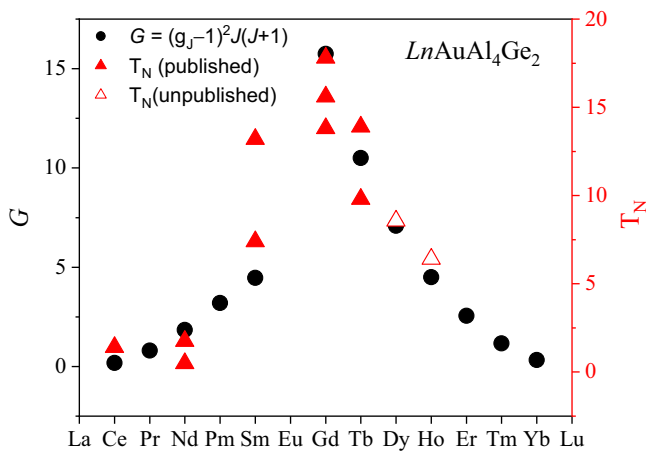


FIG. 6. Comparison between the de Gennes scaling factor G (defined in the text) and the ordering temperatures T_{N1} and T_{N2} (triangles) for the $LnAuAl_4Ge_2$ series. Data for $Ln = Ce$, Nd, Gd, and Tb are from Refs. [29–32]. Open triangles are from unpublished data [47].

leads to the modification of high-curvature Fermi surfaces due to zone-folding energy gaps, thereby producing linear magnetoresistance [51–53]. More recently, angle-resolved photoemission spectroscopy measurements also revealed the presence of nontrivial topologically protected bands [54], whose impact on the electrical transport remains to be clarified. In order to investigate these points, it will be of interest to measure the magnetoresistance of the Y, Ce, and Nd analogs, to search for Fermi surface similarities or instabilities (e.g., by detecting quantum oscillations), and to perform measurements to even higher fields to reveal the extent of linear magnetoresistance throughout the entire family.

V. CONCLUSIONS

In summary, we have shown that $\text{SmAuAl}_4\text{Ge}_2$ exhibits weak paramagnetism that strongly deviates from conventional Curie-Weiss behavior. This is described in terms of crystal electric field splitting, where the energy difference between the ground state and the first excited state is on the order of several tens of meV. Similar to other $\text{LnAuAl}_4\text{Ge}_2$ analogs, complex antiferromagnetic ordering emerges at low temperatures ($T_{N1} = 13.2$ K and $T_{N2} = 7.4$ K). This behavior is likely related to the geometrically frustrated triangular arrangement of Ln ions in the ab plane, but other factors such as complexity in the RKKY interaction may play an important role. The temperature-dependent electrical resistivity and heat capacity

indicate standard metallic behavior, although linear magnetoresistance appears within the ordered states over a wide field range. This low-temperature behavior resembles what is seen for other $\text{LnAuAl}_4\text{Ge}_2$ materials, with some noteworthy differences, including the lack of metamagnetic phase transitions. Thus, $\text{SmAuAl}_4\text{Ge}_2$ emerges as an environment for complex quantum spin states and unusual magnetotransport behaviors and invites further investigations of the entire family of materials. In particular, it will be useful to measure the order parameters (e.g., using neutron scattering), to quantify the in-plane magnetic anisotropy, to search for metamagnetic phase transitions at even larger magnetic fields, and to develop a better understanding of the Fermi surface topography and possible topology (e.g., using quantum oscillations or angle-resolved photoemission spectroscopy measurements).

ACKNOWLEDGMENTS

R.B., K.F., and O.O. were supported by the National Science Foundation through Grant No. DMR-1904361. C.B. was supported by the National High Magnetic Field Laboratory Research Experience for Undergraduates program. M.L. was supported by the U.S. Department of Energy, Basic Energy Sciences, Materials Sciences and Engineering Division under Grant No. DE-SC0021377. The National High Magnetic Field Laboratory is supported by the National Science Foundation through Grant No. DMR-1644779 and the state of Florida.

-
- [1] A. P. Ramirez, Strongly geometrically frustrated magnets, *Annu. Rev. Mater. Sci.* **24**, 453 (1994).
- [2] A. P. Ramirez, A. Hayashi, R. J. Cava, R. Siddharthan, and B. S. Shastry, Zero-point entropy in ‘spin ice,’ *Nature (London)* **399**, 333 (1999).
- [3] L. Balents, Spin liquids in frustrated magnets, *Nature (London)* **464**, 199 (2010).
- [4] Y. Zhou, K. Kanoda, and T.-K. Ng, Quantum spin liquid states, *Rev. Mod. Phys.* **89**, 025003 (2017).
- [5] P. W. Anderson, Resonating valence bonds: A new kind of insulator? *Mater. Res. Bull.* **8**, 153 (1973).
- [6] B. Bernu, C. Lhuillier, and L. Pierre, Signature of Néel order in exact spectra of quantum antiferromagnets on finite lattices, *Phys. Rev. Lett.* **69**, 2590 (1992).
- [7] O. Nagai, S. Miyashita, and T. Horiguchi, Ground state of the antiferromagnetic Ising model of general spin S on a triangular lattice, *Phys. Rev. B* **47**, 202 (1993).
- [8] F. Wang and A. Vishwanath, Spin-liquid states on the triangular and kagomé lattices: A projective-symmetry-group analysis of Schwinger boson states, *Phys. Rev. B* **74**, 174423 (2006).
- [9] M. Tamura and R. Kato, Magnetic susceptibility of β' -[Pd(dmit)₂] salts ((dmit) = 1,3-dithiol-2-thione-4, 5-dithiolate, C₃S₅): Evidence for frustration in spin-1/2 Heisenberg antiferromagnets on a triangular lattice, *J. Phys.: Condens. Matter* **14**, L729 (2002).
- [10] K. W. Plumb, J. P. Clancy, L. J. Sandilands, V. V. Shankar, Y. F. Hu, K. S. Burch, H.-Y. Kee, and Y.-J. Kim, α -RuCl₃: A spin-orbit assisted Mott insulator on a honeycomb lattice, *Phys. Rev. B* **90**, 041112(R) (2014).
- [11] A. Banerjee, C. A. Bridges, J.-Q. Yan, A. A. Aczel, L. Li, M. B. Stone, G. E. Granroth, M. D. Lumsden, Y. Yiu, J. Knolle, S. Bhattacharjee, D. L. Kovrizhin, R. Moessner, D. A. Tennant, D. G. Mandrus, and S. E. Nagler, Proximate Kitaev quantum spin liquid behaviour in a honeycomb magnet, *Nat. Mater.* **15**, 733 (2016).
- [12] M. A. McGuire, Crystal and magnetic structures in layered, transition metal dihalides and trihalides, *Crystals* **7**, 121 (2017).
- [13] E. D. L. Rienks *et al.*, Large magnetic gap at the Dirac point in Bi₂Te₃/MnBi₂Te₄ heterostructures, *Nature (London)* **576**, 423 (2019).
- [14] Y. Li, G. Chen, W. Tong, L. Pi, J. Liu, Z. Yang, X. Wang, and Q. Zhang, Rare-earth triangular lattice spin liquid: A single-crystal study of YbMgGaO₄, *Phys. Rev. Lett.* **115**, 167203 (2015).
- [15] C. A. Pocs, P. E. Siegfried, J. Xing, A. S. Sefat, M. Hermele, B. Normand, and M. Lee, Systematic extraction of crystal electric-field effects and quantum magnetic model parameters in triangular rare-earth magnets, *Phys. Rev. Res.* **3**, 043202 (2021).
- [16] M. A. Ruderman and C. Kittel, Indirect exchange coupling of nuclear magnetic moments by conduction electrons, *Phys. Rev.* **96**, 99 (1954).
- [17] K. Yosida, Magnetic properties of Cu-Mn alloys, *Phys. Rev.* **106**, 893 (1957).
- [18] T. Kasuya, A theory of metallic ferro- and antiferromagnetism on Zener’s model, *Prog. Theor. Phys.* **16**, 45 (1956).
- [19] M. Kang, S. Fang, L. Ye, H. C. Po, J. Denlinger, C. Jozwiak, A. Bostwick, E. Rotenberg, E. Kaxiras, J. G. Checkelsky, and R. Comin, Topological flat bands in frustrated kagome lattice CoSn, *Nat. Commun.* **11**, 4004 (2020).
- [20] B. C. Sales, W. R. Meier, A. F. May, J. Xing, J.-Q. Yan, S. Gao, Y. H. Liu, M. B. Stone, A. D. Christianson, Q. Zhang, and M. A.

- McGuire, Tuning the flat bands of the kagome metal CoSn with Fe, In, or Ni doping, *Phys. Rev. Mater.* **5**, 044202 (2021).
- [21] R. Brenden, L. C. Ortiz, J. R. Gomes, M. W. Morey, M. Bordelon, J. S. Mangum, I. W. H. Oswald, J. A. Rodriguez-Rivera, J. R. Neilson, S. D. Wilson, E. Ertekin, T. M. McQueen, and E. S. Toberer, New kagome prototype materials: Discovery of KV_3Sb_5 , RbV_3Sb_5 , and CsV_3Sb_5 , *Phys. Rev. Mater.* **3**, 094407 (2019).
- [22] B. R. Ortiz, S. M. L. Teicher, Y. Hu, J. L. Zuo, P. M. Sarte, E. C. Schueller, A. M. Milinda Abeykoon, M. J. Krogstad, S. Rosenkranz, R. Osborn, R. Seshadri, L. Balents, J. He, and S. D. Wilson, CsV_3Sb_5 : A Z_2 topological kagome metal with a superconducting ground state, *Phys. Rev. Lett.* **125**, 247002 (2020).
- [23] T. Kurumaji, T. Nakajima, M. Hirschberger, A. Kikkawa, Y. Yamasaki, H. Sagayama, H. Nakao, Y. Taguchi, T.-H. Arima, and Y. Tokura, Skyrmion lattice with a giant topological Hall effect in a frustrated triangular-lattice magnet, *Science* **365**, 914 (2019).
- [24] Q. Wang, S. Sun, X. Zhang, F. Pang, and H. Lei, Anomalous Hall effect in a ferromagnetic Fe_3Sn_2 single crystal with a geometrically frustrated Fe bilayer kagome lattice, *Phys. Rev. B* **94**, 075135 (2016).
- [25] Q. Wang, K. J. Neubauer, C. Duan, Q. Yin, S. Fujitsu, H. Hosono, F. Ye, R. Zhang, S. Chi, K. Krycka, H. Lei, and P. Dai, Field-induced topological Hall effect and double-fan spin structure with a c -axis component in the metallic kagome antiferromagnetic compound YMn_6Sn_6 , *Phys. Rev. B* **103**, 014416 (2021).
- [26] Y. Tokiwa, J. J. Ishikawa, S. Nakatsuji, and P. Gegenwart, Quantum criticality in a metallic spin liquid, *Nat. Mater.* **13**, 356 (2014).
- [27] X. Wu and M. G. Kanatzidis, $REAuAl_4Ge_2$ and $REAuAl_4(Au_xGe_{1-x})_2$ (RE = rare earth element): Quaternary intermetallics grown in liquid aluminum, *J. Solid State Chem.* **178**, 3233 (2005).
- [28] K. Momma and F. Izumi, VESTA 3 for three-dimensional visualization of crystal, volumetric and morphology data, *J. Appl. Crystallogr.* **44**, 1272 (2011).
- [29] S. Zhang, N. Aryal, K. Huang, K. W. Chen, Y. Lai, D. Graf, T. Besara, T. Siegrist, E. Manousakis, and R. E. Baumbach, Electronic structure and magnetism in the layered triangular lattice compound $CeAuAl_4Ge_2$, *Phys. Rev. Mater.* **1**, 044404 (2017).
- [30] M. Cong, H. Ge, L. Zhang, W. Ren, N. Zhao, T. Li, S. Wang, J. Zhu, J. Mei, Q. Zhang, J. Sheng, F. Gao, B. Li, Z. Zhang, and L. Wu, Magnetic phase diagram and multiple field-induced states in the intermetallic triangular-lattice antiferromagnet $NdAuAl_4Ge_2$ with Ising-like spins, *Phys. Rev. Mater.* **7**, 024423 (2023).
- [31] K. Feng, I. A. Leahy, O. Oladehin, K. Wei, M. Lee, and R. Baumbach, Magnetic ordering in $GdAuAl_4Ge_2$ and $TbAuAl_4Ge_2$: Layered compounds with triangular lanthanide nets, *J. Magn. Magn. Mater.* **564**, 170006 (2022).
- [32] I. A. Leahy, K. Feng, R. Dery, R. Baumbach, and M. Lee, Field-induced magnetic states in the metallic rare-earth layered triangular antiferromagnet $TbAuAl_4Ge_2$, *Phys. Rev. B* **106**, 094426 (2022).
- [33] S. Shin, V. Pomjakushin, L. Keller, P. F. S. Rosa, U. Stuhr, C. Niedermayer, R. Sibille, S. Toth, J. Kim, H. Jang, S.-K. Son, H.-O. Lee, T. Shang, M. Medarde, E. D. Bauer, M. Kenzelmann, and T. Park, Magnetic structure and crystalline electric field effects in the triangular antiferromagnet $CePtAl_4Ge_2$, *Phys. Rev. B* **101**, 224421 (2020).
- [34] J. H. Van Vleck, *The Theory of Electric and Magnetic Susceptibilities* (Oxford University Press, Oxford, 1965), p. 245.
- [35] S. Singh, S. Saha, S. K. Dhar, R. Suryanarayanan, A. K. Sood, and A. Revcolevschi, Manifestation of geometric frustration on magnetic and thermodynamic properties of the pyrochlores $Sm_2X_2O_7$ ($X = Ti, Zr$), *Phys. Rev. B* **77**, 054408 (2008).
- [36] S. Sanada, Y. Aoki, H. Aoki, A. Tsuchiya, D. Kikuchi, H. Sugawara, and H. Sato, Exotic heavy-fermion state in filled skutterudite $SmOs_4Sb_{12}$, *J. Phys. Soc. Jpn.* **74**, 246 (2005).
- [37] W. M. Yuhasz, N. A. Frederick, P. C. Ho, N. P. Butch, B. J. Taylor, T. A. Sayles, M. B. Maple, J. B. Betts, A. H. Lacerda, P. Rogl, and G. Giester, Heavy-fermion behavior, crystalline electric field effects, and weak ferromagnetism in $SmOs_4Sb_{12}$, *Phys. Rev. B* **71**, 104402 (2005).
- [38] R. Gumenuik, M. Schöneich, A. Leithe-Jasper, W. Schnelle, M. Nicklas, H. Rosner, A. Ormeci, U. Burkhardt, M. Schmidt, U. Schwarz, M. Ruck, and Y. Grin, High-pressure synthesis and exotic heavy-fermion behaviour of the filled skutterudite $SmPt_4Ge_{12}$, *New J. Phys.* **12**, 103035 (2010).
- [39] R. Higashinaka, T. Maruyama, A. Nakama, R. Miyazaki, Y. Aoki, and H. Sato, Unusual field-insensitive phase transition and Kondo behavior in $SmTi_2Al_{20}$, *J. Phys. Soc. Jpn.* **80**, 093703 (2011).
- [40] A. Menth, E. Buehler, and T. H. Geballe, Magnetic and semi-conducting properties of SbB_6 , *Phys. Rev. Lett.* **22**, 295 (1969).
- [41] M. Dzero, K. Sun, V. Galitski, and P. Coleman, Topological Kondo insulators, *Phys. Rev. Lett.* **104**, 106408 (2010).
- [42] H. C. Hamaker, L. D. Woolf, H. B. MacKay, Z. Fisk, and M. B. Maple, Coexistence of superconductivity and antiferromagnetic order in $SmRh_4B_4$, *Solid State Commun.* **32**, 289 (1979).
- [43] A. Jayaraman, V. Narayanamurti, E. Bucher, and R. G. Maines, Continuous and discontinuous semiconductor-metal transition in samarium monochalcogenides under pressure, *Phys. Rev. Lett.* **25**, 1430 (1970).
- [44] M. Bouvier, P. Lethuillier, and D. Schmitt, Specific heat in some gadolinium compounds. I. Experimental, *Phys. Rev. B* **43**, 13137 (1991).
- [45] Quantum Design, Slope analysis of relaxation curves, in *Physical Property Measurement System Heat Capacity Option User's Manual*, 19th ed. (Quantum Design, San Diego, 2010), Chap. 4.3.4; Slope analysis, in *Physical Property Measurement System Heat Capacity Option User's Manual*, 19th ed. (Quantum Design, San Diego, 2010), Chap. 4.6.2.
- [46] S. Blundell, Isolated magnetic moments, in *Magnetism in Condensed Matter* (Oxford University Press, Oxford, 2001), p. 34.
- [47] K. Feng and R. Baumbach (unpublished data).
- [48] P. G. de Gennes, Interactions indirectes entre couches 4f dans les métaux de terres rares, *J. Phys. Radium* **23**, 510 (1962).
- [49] W. C. Koehler, Magnetic properties of rare-earth metals and alloys, *J. Appl. Phys.* **36**, 1078 (1965).
- [50] W. Selke, The ANNNI model-Theoretical analysis and experimental application, *Phys. Rep.* **170**, 213 (1988).
- [51] K. K. Kolincio, M. Roman, and T. Klimczuk, Enhanced mobility and large linear nonsaturating magnetoresistance in the magnetically ordered states of $TmNiC_2$, *Phys. Rev. Lett.* **125**, 176601 (2020).

- [52] S. Tsuda, C. L. Yang, Y. Shimura, K. Umeo, H. Fukuoka, Y. Yamane, T. Onimaru, T. Takabatake, N. Kikugawa, T. Terashima, H. T. Hirose, S. Uji, S. Kittaka, and T. Sakakibara, Metamagnetic crossover in the quasikagome Ising Kondo-lattice compound CeIrSn, *Phys. Rev. B* **98**, 155147 (2018).
- [53] Y. Feng, Y. Wang, D. M. Silevitch, J.-Q. Yan, R. Kobayashi, M. Hedod, T. Nakamad, Y. Onuki, A. V. Suslove, B. Mihaila, P. B. Littlewood, and T. F. Rosenbaum, Linear magnetoresistance in the low-field limit in density-wave materials, *Proc. Natl. Acad. Sci. USA* **116**, 11201 (2019).
- [54] C. Zhang, Y. Wang, F. Zhang, H. Rong, Y. Cai, L. Wang, X.-M. Ma, S. Guo, Z. Chen, Y. Wang, Z. Jiang, Y. Yang, Z. Liu, M. Ye, J. Lin, J. Mei, Z. Hao, Z. Xie, and C. Chen, Multiple surface states, nontrivial band topology and anti-ferromagnetism in GdAuAl₄Ge₂, *Chin. Phys. B* **32**, 077401 (2023).